Title

Erythrocyte-Derived Theranostic Nanoplatforms for Near Infrared Fluorescence Imaging and Photodestruction of Tumors

Journal
ACS Applied Materials & Interfaces, 10(33)

ISSN
1944-8244

Authors
Burns, Joshua M
Vankayala, Raviraj
Mac, Jenny T
et al.

Publication Date
2018-08-22

DOI
10.1021/acsami.8b08005

Peer reviewed

Erythrocyte-Derived Theranostic Nanoplatforms for Near Infrared Fluorescence Imaging and Photodestruction of Tumors

Journal:	*ACS Applied Materials & Interfaces*
Manuscript ID	am-2018-08005b.R2
Manuscript Type:	Article
Date Submitted by the Author:	n/a
Complete List of Authors:	Burns, Joshua; University of California, Riverside, Bioengineering Vankayala, Raviraj; University of California, Riverside, Bioengineering Mac, Jenny; University of California, Riverside, Bioengineering Anvari, Bahman; University of California, Riverside, Department of Bioengineering

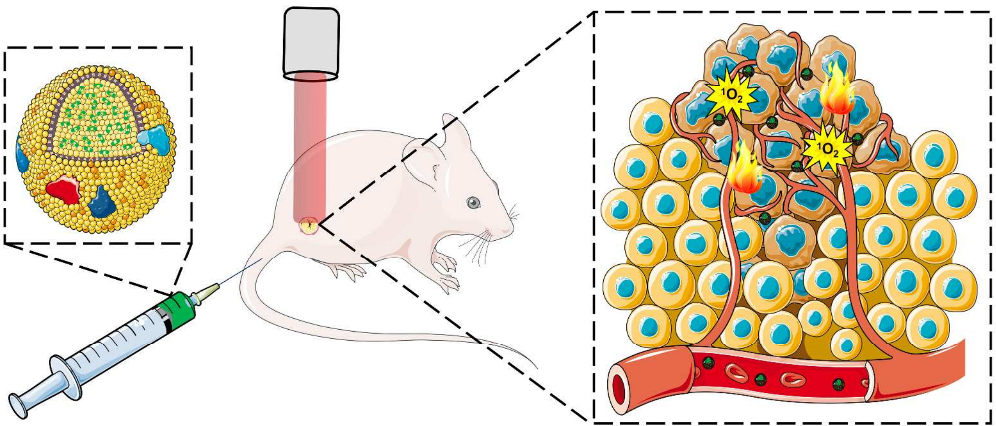

Erythrocyte-derived optical nanoparticles for fluorescent imaging and photo-destruction of tumors

338x145mm (300 x 300 DPI)

Erythrocyte-Derived Theranostic Nanoplatforms for Near Infrared Fluorescence Imaging and Photodestruction of Tumors

Joshua M. Burns, [†] Raviraj Vankayala[†], Jenny T. Mac[‡], Bahman Anvari[†, ‡*]

[†]Department of Bioengineering, University of California, Riverside, 900 University Ave., Riverside, CA 92521, USA

[‡]Department of Biochemistry, University of California, Riverside, 900 University Ave., Riverside, CA 92521, USA

*E-mail: anvarib@ucr.edu

ABSTRACT: Nanoparticles activated by near infrared (NIR) excitation provide a capability for optical imaging and photo-destruction of tumors. We have engineered optical nano-constructs derived from erythrocytes, which are doped with the FDA-approved NIR dye, indocyanine green (ICG). We refer to these constructs as NIR erythrocyte-mimicking transducers (NETs). Herein, we investigate the photo-theranostic capabilities of NETs for fluorescence imaging and photo-destruction of SKBR3 breast cancer cells, and subcutaneous xenograft tumors in mice. Our cellular studies demonstrate that NETs are internalized by these cancer cells, and localized to their lysosomes. As evidenced by NIR fluorescence imaging and *in vivo* laser irradiation studies, NETs remain available within tumors at 24 hours post intravenous injection. In response to continuous wave 808 nm laser irradiation at intensity of 680 mW/cm^2 for 10-15 minutes, NETs mediate the destruction of cancer cells and tumors in mice through synergistic photochemical and photothermal effects. We demonstrate that NETs are effective in mediating photo-activation of Caspase-3 to induce tumor apoptosis. Our results provide support in effectiveness of NETs as theranostic agents for fluorescence imaging and photo-destruction of tumors, and their role in photo-induced apoptosis initiated by their localization to lysosomes.

KEYWORDS: *apoptosis, lysosomes, indocyanine green, red blood cells, photodynamic therapy, photothermal therapy*

INTRODUCTION

Light-activated materials present a potential theranostic platform for image-guided phototherapy.[1–3] In particular, use of near infrared (NIR) wavelengths (≈ 750-1450 nm) is especially advantageous since relatively deep (≈ 2-3 cm) optical imaging and phototherapy can be achieved due to reduced light absorption and scattering by endogenous constituents. To-date, indocyanine green (ICG) remains as the only NIR-activated agent approved by FDA for specific clinical applications including ophthalmic angiography, cardiocirculatory measurements, assessment of hepatic function and blood flow evaluation.[4,5] ICG has also been investigated for potential applications ranging from sentinel lymph node mapping in patients with different types of cancer to imaging intracranial aneurysm and cerebral arteriovenous malformations.[6–11]

In addition to its optical imaging capabilities, ICG has also been investigated as a photosensitizer for photodynamic therapy of choroidal melanomas and breast adenocarcinomas,[12,13] as well as a photothermal agent for treatment of port wine stains.[14] However, ICG's major drawbacks are its short plasma half-life (≈ 3-5 minutes) and non-specific interactions with various biological macromolecules, particularly serum albumin and high density lipoproteins. To overcome these limitations, ICG has been encapsulated within various constructs, including micelles, liposomes, silica and synthetic polymers.[15–20]

Use of mammalian cells such as erythrocytes, lymphocytes, and macrophages, or constructs derived from them, are receiving increased attention as delivery platforms due to increased circulation time and biocompatibility.[21–25] For example, Hu et al reported that nano-constructs (≈ 80 nm diameter) composted of poly (lactic-co-glycolic acid) core coated with erythrocyte-derived membranes were retained in blood for three days with circulation half-life of

≈ 8 hours in mice.[26] Piao et al have reported that the circulation half-life of gold nanocages cloaked with erythrocyte membranes (≈ 90 nm diameter) was ≈ 9.5 hours.[24] Rao et al did not observe systemic toxicity 15 days after intravenous injection of erythrocyte membrane-coated upconversion nanoparticles in mice.[23]

We previously provided the first report on the engineering of nano-sized vesicles derived from erythrocytes loaded with ICG, and their utility for fluorescence imaging and photo-destruction of human dermal microvascular endothelial (HDME) cells.[27] We refer to these constructs as NIR erythrocyte-mimicking transducers (NETs) since once activated by NIR light, NETs can transduce the absorbing photons energy to generate heat, emit fluorescence, or mediate production of reactive oxygen species (ROS). Herein, we investigate the photo-theranostic capabilities of NETs for near infrared fluorescence imaging and photo-destruction of cancer cells and subcutaneous xenograft tumors in mice. We demonstrate that NETs remain available within tumors at 24 hours post intravenous injection, and mediate the destruction of cancer cells and tumors through synergistic photochemical and photothermal effects in response to continuous wave laser irradiation. We report for the first time that NETs are localized to cancer cells lysosomes, and upon photo-excitation can induce Caspase-3 activation, leading to tumor apoptosis.

RESULTS AND DISCUSSION

Characterization of NETs. The mean peak hydrodynamic diameter of NETs as estimated by dynamic light scattering (DLS) was ≈ 79 nm (Figure 1a). We used lognormal fits to estimate the mean ± standard deviation (SD) diameter of NETs as 85 ± 1 nm. We have previously published transmission electron[27] and scanning electron[28] microscopic images of NETs, and demonstrated that DLS-based measurements of NETs' diameters are consistent with those made by electron microscopy. The polydispersibility index (PDI) value for this set of NETs was 0.2, meaning that the standard deviation in diameter is 20% of the mean value. Nanoparticles with PDI values in the range of 0.1~0.4 are considered as moderately polydispersed.[29] Since the hydrodynamic diameters of NETs are < 200 nm, they are likely to be effective for extravasation into tumors through the enhanced permeability and retention (EPR) effect, induced by the leaky tumor vasculature and impaired lymphatic drainage.[30,31]

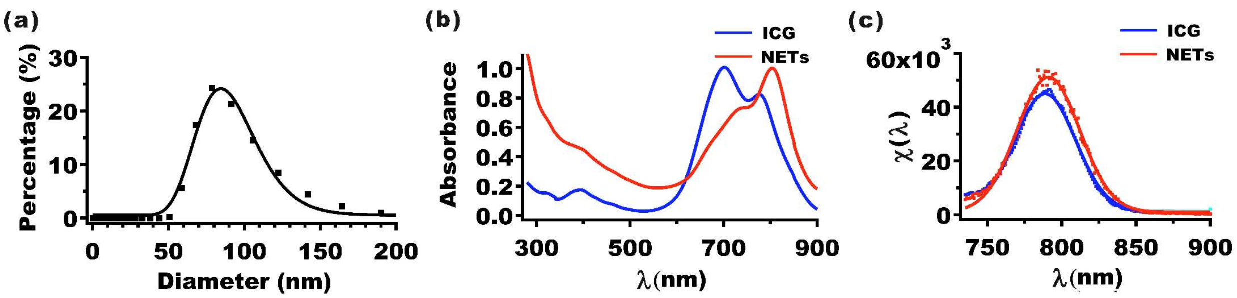

Figure 1. Characterization of NETs. (a) Hydrodynamic diameter distribution of NETs as determined by DLS. Circles and error bars (too small to be seen) represent the mean and standard deviations of diameters, respectively (n = 4 measurements). The estimated mean diameter as determined from the lognormal fits (solid curves) is ≈ 85 nm. (b) Absorption spectra of 13 μM free ICG, and NETs ($[ICG_{NETs}]$ ≈ 10 μM). (c) Normalized fluorescence emission spectra ($\chi(\lambda)$) (see equation 1)) (circles) and Gaussian fits (solid curves) of 4 μM free ICG and NETs ($[ICG_{NETs}]$ ≈ 2 μM) in response to photo-excitation at 720±2.5 nm. Solvent used in spectral recordings was 310 mOsm PBS.

The absorption spectrum of free 13 μM ICG dissolved in ≈ 310 mOsm phosphate buffer saline (PBS) (defined as the 1X PBS), and NETS fabricated using 1.1 mM ICG in the loading buffer are shown in Figure 1b. The free ICG equivalent concentration loaded into these NETs

[ICG_{NETs}] was estimated as ≈ 10 μM (see EXPERIMENTAL SECTION). Absorption spectrum of free ICG exhibited primary and secondary peaks at 698 and 776 nm, associated with the H-like aggregate and monomeric forms of ICG, respectively.[32] In contrast, NET, suspended in 1X PBS, showed a dominant spectral peak at 804 nm, suggesting that the monomeric ICG was the dominant form within these NETs. The bathochromic (red) spectral shift in the monomeric absorption of free ICG from 776 nm to 804 nm in NETs is consistent with our previous results.[27,28,33] This shift can be attributed to the binding of ICG molecules to phospholipids and membrane proteins of the NETs, causing a change in the molecular energy levels of ICG, as well as the local solvent environment surrounding ICG within the NETs.[32,34]

In response to photo-excitation at 720 ± 2.5 nm, the normalized fluorescence emission spectra ($\chi(\lambda)$) (see equation 1) of 4 μM free ICG and NETs ([ICG_{NETs}] ≈ 2 μM) showed respective peaks at 792 and 796 nm, associated with the monomer form respectively (Figure 1c). The normalized fluorescence emission spectra had a similar bathochromic shift from 792 nm (associated with monomer form of free ICG) to 796 nm (associated with emission from the monomeric form of ICG in NETs). Peak value of $\chi(\lambda)$ for NETs was ≈ 15% higher than that of free ICG. This increase may be due to reduced self-aggregation of ICG as a result of its binding to proteins and lipids in the membrane shell of NETs. Similar fluorescent enhancement has been reported for ICG binding to lipids,[17] proteins in fetal bovine serum,[32] and albumin.[35]

Photostability and NETs-mediated singlet oxygen generation. To gain insight on photostability of ICG in both free and nano-encapsulated formulations, we acquired their respective absorption spectra immediately after being laser irradiated at 808 nm with incident intensity (I_o) of 680 mW/cm^2 for up to 15 minutes (Figure 2a). We prepared solutions of free ICG (22 μM) and NETs ([ICG_{NETs}] ≈ 18 μM) in 1X PBS so that the absorbance values for both free ICG and NETs at 808 nm were 1.8. With increasing laser irradiation times, there were corresponding reductions in the absorption spectra (Figure 2a). These reductions can be attributed to photo-induced chemical modification of ICG molecules to produce a leuco form of the dye with converted sp^2 to sp^3 carbon hybridization, and/or induce cleavage of the π–conjugation along the polyene segment of the dye while keeping the aromatic benzoindotricarbocyanine moieties intact.[27] At 808 nm, free ICG had the lowest percentage decrease in its absorbance values as compared with NETs (Figure 2b). For example, after 15 minutes of irradiation, the 808 nm absorbance values of free ICG and NETs irradiated at 680 mW/cm^2 decreased by 26.2, and 60.0%, respectively. Greater reductions in 808 nm absorbance values of NETs upon laser irradiation may be due to induced molecular conformational changes in ICG as a result of nano-encapsulation.

We used 1,3-diphenylisobenofuran (DPBF) as a probe to assess the generation of singlet oxygen ($^1O_2$) in response to 808 nm photo-excitation of free ICG and NETs (see EXPERIMENTAL SECTION). Laser irradiation of DMF-dissolved DPBF at I_o = 680 mW/cm^2 for up to 80 seconds did not alter the absorbance value at 411 nm (Figure 2c), confirming that there was no photo-induced production of $^1O_2$ in the absence of NIR absorbing molecules or particles. However, in presence of free ICG or NETs, the normalized DPBF absorbance at 411 nm progressively decreased with increased 808 nm laser irradiation time (Figure 2c). Generation of $^1O_2$ is consistent with the type II photochemistry where the intersystem crossing of ICG (in free or nano-encapsulated form) to the excited triplet state is followed by energy transfer to the ground state molecular oxygen, producing $^1O_2$.

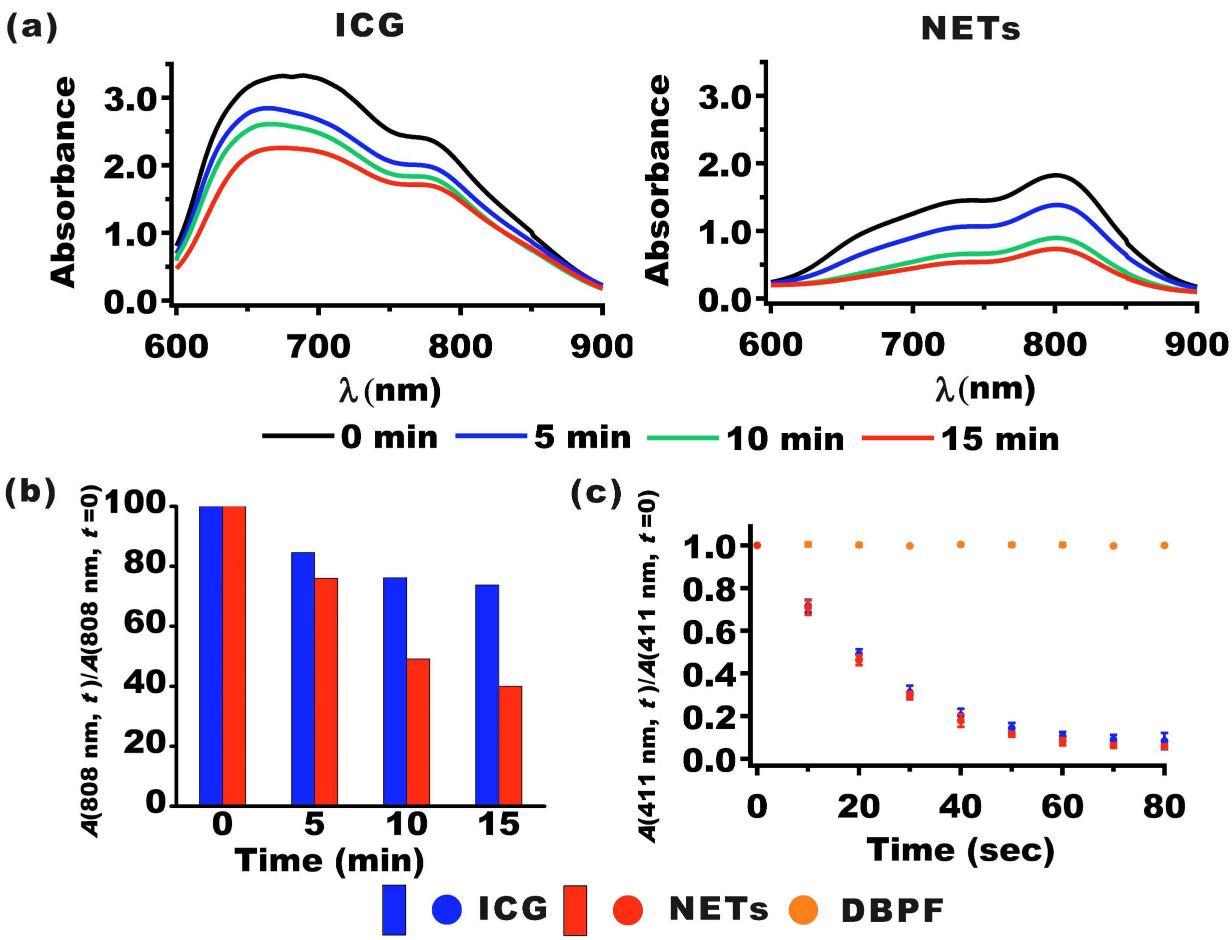

Figure 2. Photostability and $^1O_2$ generation of NETs in solution. (a) Absorption spectra of 22 μM free ICG, and NETs ($[ICG_{NETs}] \approx 18$ μM) before and after 808 nm laser irradiation (I_o = 680 mW/cm^2) for 5, 10, and 15 minutes. (b) Normalized 808 nm absorbance values for ICG and NETs as a function of 808 nm laser irradiation time. (c) Normalized 411 nm absorbance values for solutions containing 10 μM DPBF without, or with 11 μM ICG or NETs ($[ICG_{NETs}] \approx 18$ μM) as a function of 808 nm laser irradiation time. Data points and error bars in panel (c) represent the mean and SDs for n = 4 samples.

Fluorescence imaging of SKBR3 breast cancer cells incubated with NETs. SKBR3 human breast cancer cells were incubated at 37 °C with PBS (negative control), 44 μM free ICG (positive control) or NETs ([ICG_{NETs}] ≈ 36 μM) for three hours. Following incubation, cells were washed, and then fluorescently imaged. While there were none or minimal NIR fluorescence emission from SKBR3 cells incubated with PBS or free ICG, NETs-incubated cells emitted NIR fluorescence (Figure 3a).

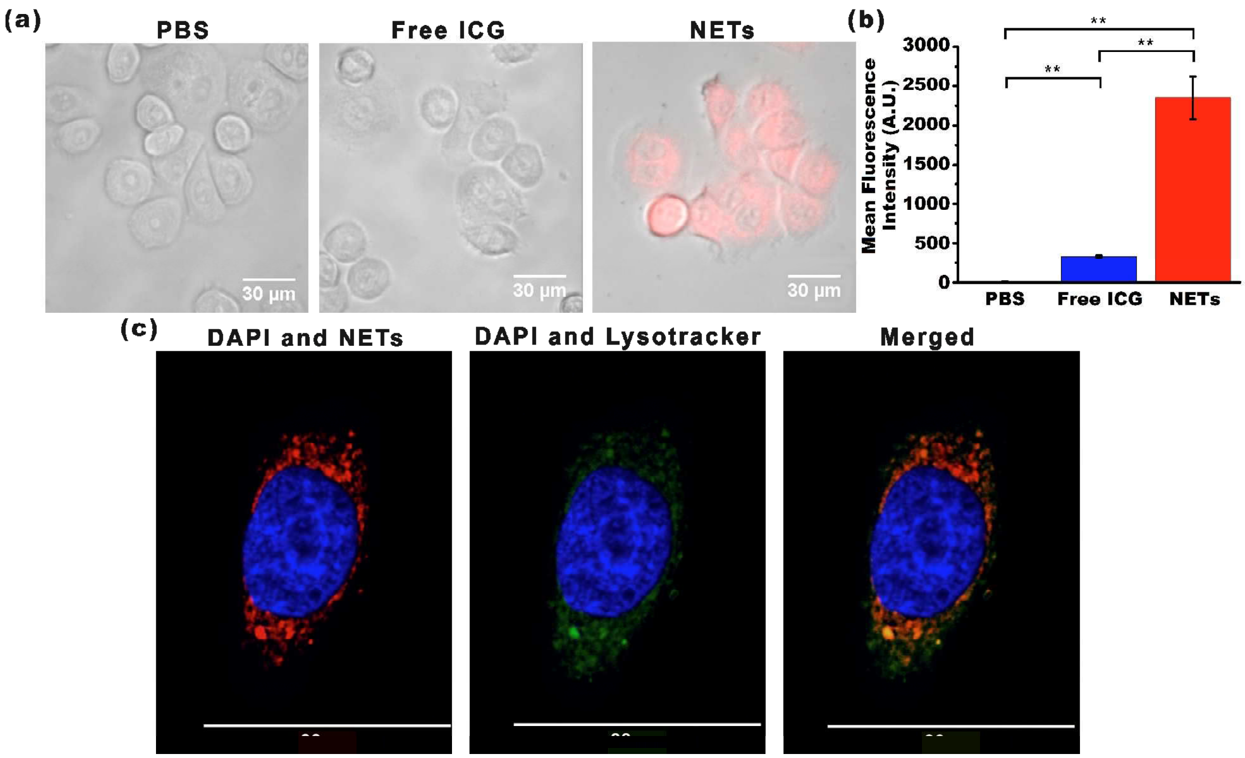

Figure 3. Uptake of NETs by SKBR3 cancer cells. (a) Merged bright-field and fluorescent images of SKBR3 cancer cells following three hours of incubation at 37 °C with PBS, 44 μM free ICG or NETs ([ICG_{NETs}] ≈ 36 μM). Images are falsely colored. Red channel: NIR emission due to ICG; Gray channel: bright-field. (b) Uptake analysis of SKBR3 cells by flow cytometry. Geometric mean fluorescence intensity (n = 3 different samples) (**) $p < 0.01$. (c) Laser scanning confocal fluorescent images of a SKBR3 cell following three hours of incubation at 37 °C with NETs. Images are falsely colored. Blue channel: DAPI; Green channel: Lysotracker; Red channel: NIR emission due to ICG from NETs.

Flow cytometry results confirmed that the mean fluorescence intensity of cells incubated with NETs were significantly higher than those associated with cells incubated with free ICG or PBS (n = 3, $p < 0.01$) (Figure 3b). These results further validate that NETs were effectively uptaken by the cells, whereas most of ICG was removed as a result of washing the cells. These results demonstrate that NETs serve as an effective platform to deliver their cargo (ICG) to cancer cells.

To determine the cellular localization of NETs, we used 4',6-diamidino-2-phenylindole (DAPI) and Lysotracker, fluorescent probes that respectively stain the nucleus and lysosomes, and imaged the cells by laser scanning confocal fluorescence microscopy (LSCFM) (Figure 3c). Lysotracker and ICG fluorescence from NETs spatially overlapped, suggesting that NETs were localized to lysosomes of the cells, and positioned at the periphery of the nucleus. Our analysis of the images indicated Pearson's value of $R = 0.99$, confirming that the intensity distributions were highly correlated. Similarly, Costes' P value of 1.00 confirmed the co-localization of the intensities from each pixel. Although not investigated here, it is possible that NETs may also accumulate in mitochondria. For example, it has been demonstrated that an analog form of ICG, consisting of a cyclohexenyl substitution in the middle of the polymethine linker and two asymmetrical amphipathic N-alkyl side chains, accumulated in the mitochondria of MCF-7 and 4T1 breast cancer cells.[36] In another study, localization of magnetic complex nanoparticles loaded with ICG to the mitochondria of A549 adenocarcinomic alveolar basal epithelial cell line was reported.[37]

Laser irradiation of SKBR3 breast cancer cells incubated with NETs. SKBR3 cells were incubated at 37 °C with PBS (negative control), 176 μM free ICG (positive control) or NETs ($[ICG_{NETs}] \approx 144$ μM) for three hours. Following incubation, cells were washed and then irradiated at 808 nm for 15 minutes using I_o = 680 mW/cm^2. We evaluated the viability of the cells following laser irradiation. Cells were stained with Calcein acetoxymethyl (AM) and ethidium homodimer-1 (EthD-1) to fluorescently visualize the live and dead cells, respectively (Figure 4a). In response to laser irradiation, ≈ 93% of ICG-treated SKBR3 cells remained viable. However, only 32% of NETs-treated cells were viable after laser irradiation at these parameters (Figure 4b).

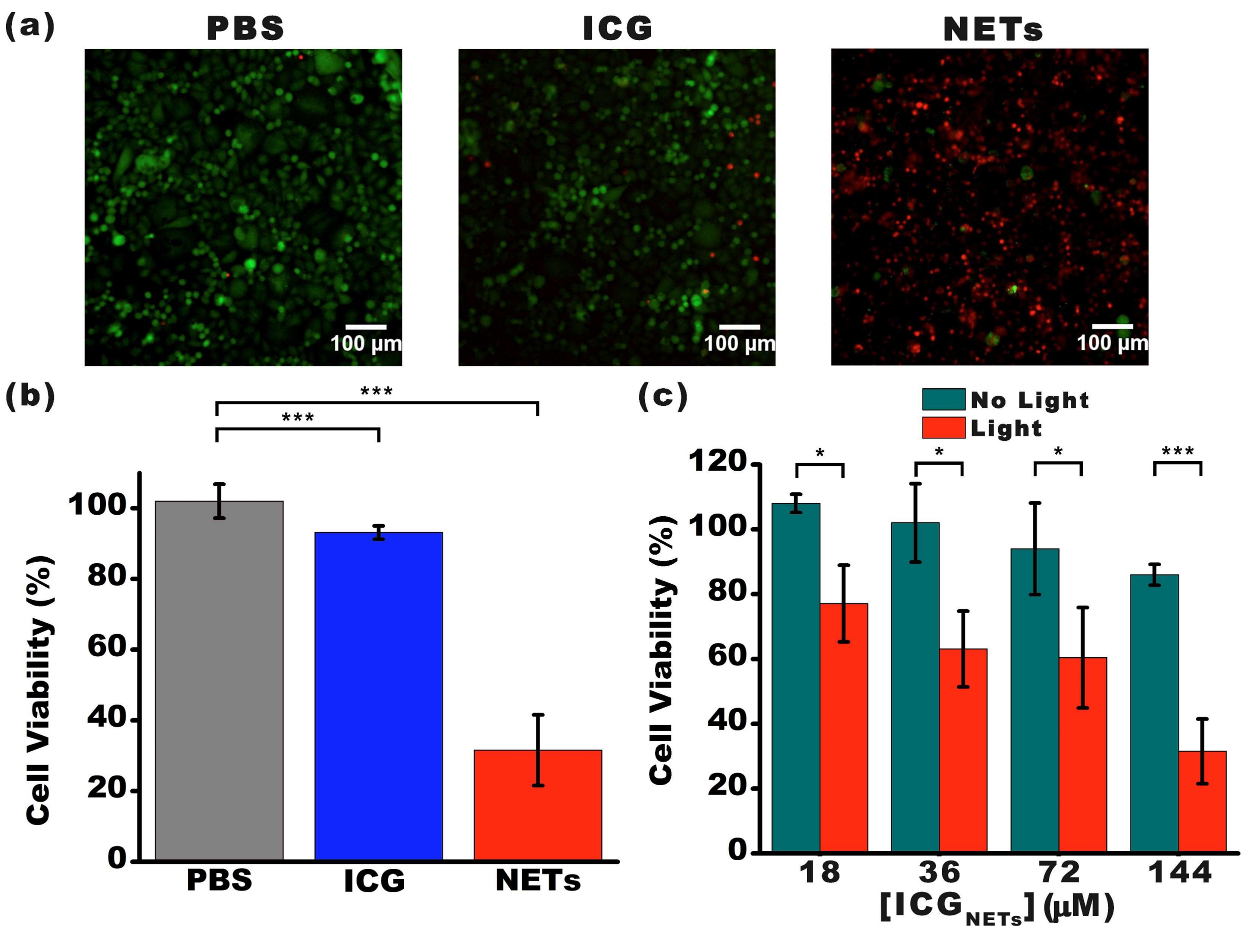

Figure 4. Photo-destruction of SKBR3 cancer cell *in vitro.* (a) Fluorescent images of SKBR3 cancer cells incubated with PBS (negative control), 176 µM free ICG (positive control), and NETs ([ICG_{NETs}] ≈ 144 µM) for three hours at 37°C and followed by 808 nm laser irradiation at

I_o = 680 mW/cm^2 for 15 minutes. Live cells were identified by the Calcein AM stain, and falsely colored in green. Dead cells in response to laser irradiation were identified using the Ethidium homodimer-1 stain, and falsely colored in red. (b) Percentage viability of SKBR3 cells as a function of incubation agent. (c) Percentage viability of SKBR3 cells as a function of [ICG_{NETs}]. In panels (b) and (c), statistically significant differences are indicated as (*) $p < 0.05$ and (***) $p < 0.001$ (n = 3 samples for each treatment).

We also evaluated the effects of [ICG_{NETs}] on photo-destruction of SKBR3 cells. The fraction of cell death progressively increased as [ICG_{NETs}] increased (Figure 4c). With increased [ICG_{NETs}] from 18 μM to 144 μM, the fractions of cells death increased from 23% to 69% for SKBR3 cells incubated with NETs.

To investigate if ROS production was a contributing mechanism to photo-induced destruction of SKBR3 cells, we used the molecular 2,7-dichlorofluorescein diacetate (DCFH-DA) (see EXPERIMENTAL SECTION). Cells incubated with NETs showed dichlorofluorescein (DCF) fluorescence whereas the incubation of cells with PBS or ICG did not result in any noticeable DCF fluorescence emission (Figure 5a). These results indicate that NETs were uptaken by SKBR3 cancer cells, and mediated ROS production in response to laser irradiation.

To determine if ROS included $^1O_2$ as a constituent, we used sodium azide as an $^1O_2$ quencher (see EXPERIMENTAL SECTION).[38] Upon pre-treatment with sodium azide, the DCF fluorescence emission from SKBR3 cells incubated with NETs was quenched after laser irradiation, indicating the DCF emission from cells not treated with sodium azide was associated with $^1O_2$ production in response to laser irradiation.

Collectively, our *in vitro* results based on analysis of cell viability (Figure 4) and the use of molecular probes for ROS detection (Figure 5) support the presence of a photo-chemical mechanism in destruction of cancer cells incubated with NETs and laser-irradiated at 808 nm using I_o = 680 mW/cm^2 for 15 minutes.

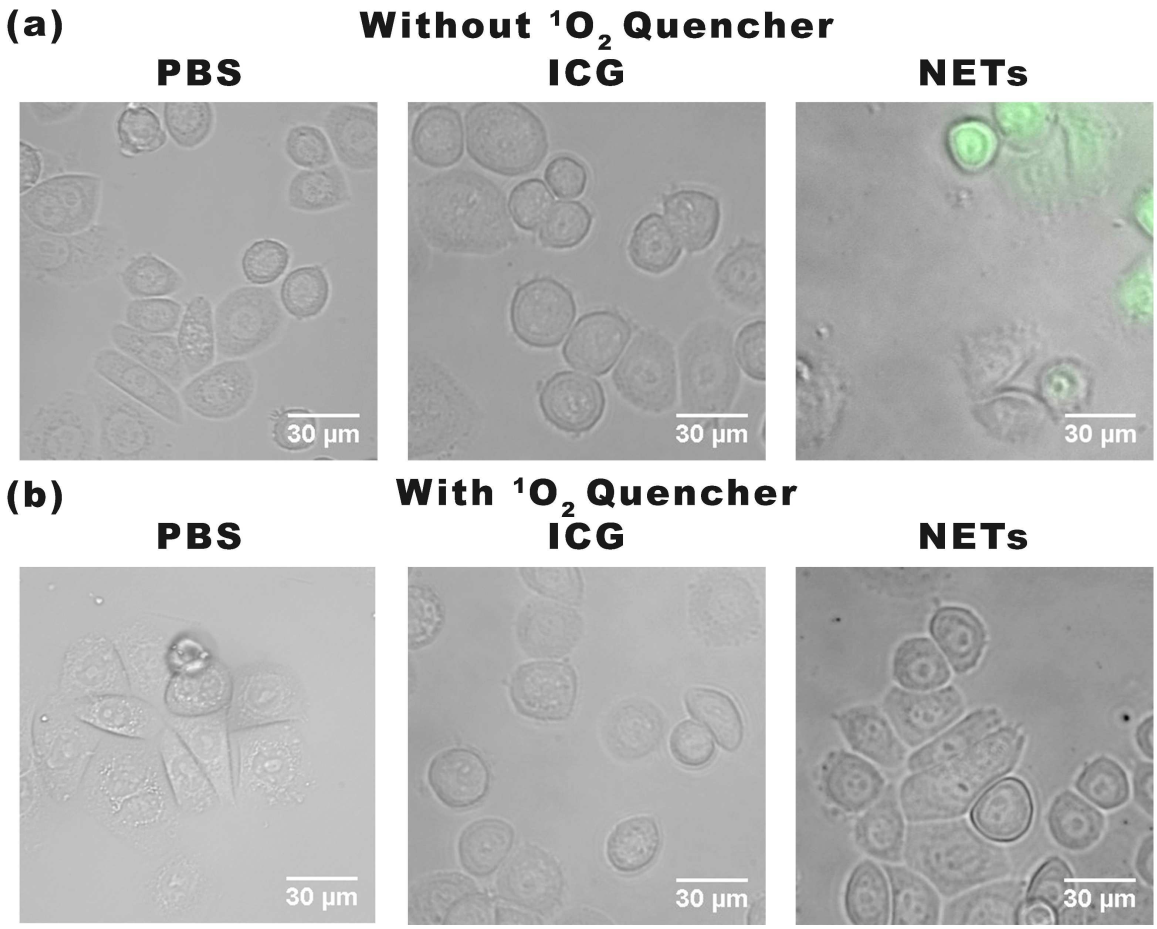

Figure 5. Detection of ROS generation by cell imaging. We present merged bright-field and DCF fluorescence images of SKBR3 cancer cells incubated with PBS, 44 μM free ICG, or NETs ([ICGNETs] ≈ 36 μM) for three hours and subsequently irradiated at 808 nm for 15 minutes at I_o = 680 mW/cm^2. Images correspond to (a) without and (b) and with application of $^1O_2$ quencher, sodium azide. Images are falsely colored. Gray channel: bright-field. Green channel: fluorescence emission from DCF.

NIR fluorescence imaging and laser irradiation of tumors. We investigated the efficacy of NETs in NIR fluorescence imaging of tumors. Tumors were extracted 24 hours after tail vein injection of PBS (control) or NETs ([ICG_{NETs}] ≈ 980 μM), and were immediately imaged by NIR photo-excitation and collecting the fluorescence emission. NETs offered the capability to image the tumor (Figure 6a), indicating that they were present within the tumor at 24 hours post-injection. These results show that encapsulation of ICG within erythrocyte-derived nano-vesicles provided an effective method to prolong the circulation of ICG, and making it available for an intended application (e.g., tumor imaging) for at least 24 hours.

We assessed the capability of NETs in mediating photo-destruction of xenograft tumors implanted subcutaneously in mice. Laser irradiation was done 24 hours after intravenous injection of NETs via the tail vein. To investigate if there was a photothermal effect during laser irradiation, we recorded the *in vivo* temperature changes using a thermocouple needle probe inserted at ≈ 1 mm below the skin and ≈ 2 mm outside the laser-irradiated spot. Laser irradiation at I_o = 680 mW/cm^2 resulted in temperature rise of ≈ 11°C at the end of the 10 minutes of irradiation time (Figure 6b). This temperature rise under-estimates the actual temperature distributions within the tumor, and is a measure of the heat diffusion from the irradiated tumor site. Nevertheless, these measurements suggest that there was a photothermal effect during laser irradiation.

To investigate the presence of cellular apoptosis in response to laser irradiation, some of the tumors were extracted immediately after laser irradiation, and imaged by fluorescent immuno-staining to detect the presence of Caspase-3. As evidenced by fluorescence emission, there was Caspase-3 activation in mice injected with NETs and irradiated at 680 mW/cm^2 for 10 minutes (Figure 6c). Analysis of these images confirmed that NETs were effective in mediating photo-induced activation of Capase-3 as evidenced by statistically significant higher values of fluorescence intensity associated with Caspase-3 (Figure 6d). Results of *in vivo* laser irradiation of tumors provide further evidence that NETs remained in circulation for at least 24 hours.

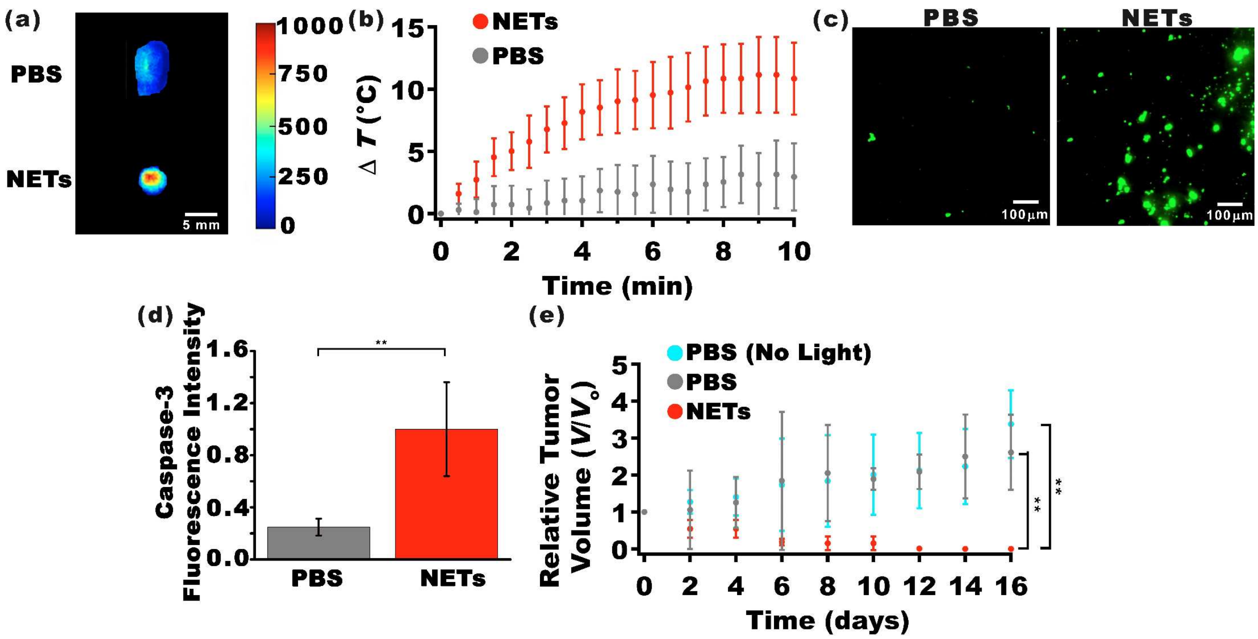

Figure 6. NIR fluorescence imaging and photo-destruction of xenograft tumors in mice. (a) NIR fluorescence images of tumors extracted 24 hours after tail injection of PBS (top panel), and NETs ([ICG_{NETs}] ≈ 980 μM) (bottom panel). Scale bar on the right corresponds to fluorescent intensity (photo-excitation at 700 ± 30 nm, and emission > 810 nm collected). (b) Temperature rise as a function of laser irradiation time as measured by a thermocouple needle probe placed ≈ 1 mm below skin surface and ≈ 2 mm outside the irradiated spot. (c) Fluorescent images of sectioned tumors by immunostaining using FITC-labeled Caspase-3 antibody. (d) Fluorescence emission intensity associated with FITC-labeled Caspase-3 antibody as the apoptosis indicator following laser irradiation. (e) Estimated relative change in tumor volumes (V) of non-orthotopic xenograft tumors in mice with respect to the volumes at time zero (V_0). Time zero is with respect to the day of laser irradiation. Mice were injected via the tail vein with either 100 μL of PBS, or

NETs ([ICG_{NETs}] ≈ 980 μM). Laser Irradiation was done 24 hours post injection of NETs or PBS. Irradiation parameters were: 808 nm; spot size = 9 mm; irradiation time = 10 min, I_o = 680 mW/cm^2. In panels (b) and (e), n = 4 mice for each administered agent. In panel (d), n = 5 images from different sections of same tumors for each administered agent (statistically significant difference at (**) $p < 0.01$).

In response to laser irradiation at I_o = 680 mW/cm^2 in conjunction with NETs, we observed reductions in tumor volumes as early as two days post-laser irradiation (Figure 6e). By 10 days post-irradiation, tumor volumes were nearly zero. In contrast, laser irradiation in the absence of NETs was associated with growths in tumor volumes, indicating the effectiveness of NETs in mediating photo-destruction of tumors.

Some important aspects of this study were the findings that: (1) NETs were localized to lysosomes as evidenced by LSCFM results (Figure 3); and (2) NETs mediated photo-activation of Caspase-3 in tumors (Figures 6c,d). These results indicate that lysosomal localization of NETs with subsequent laser irradiation, at the indicated parameters, can induce cellular apoptosis. Photo-induced damage to lysosomes membranes leads to release of cathepsin proteases and other hydrolytic enzymes into the cytosol[39] to activate apoptosis mediator proteins.[40] Pro-apoptotic mediators include a sub-group of B-cell lymphoma 2 (BCL-2) family of proteins.[41] Bid, is a member of the BCL-2 sub-group containing only the BH3 domain, which is cleaved by proteases to truncated Bid (tBid).[42] Upon translocation to the outer membranes of mitochondria, tBid can directly promote mitochondrial outer membrane permeabilization (MOMP),[43,44] or play a role in recruitment of cytosolic Bax, another member of the pro-apoptotic BCL-2 group, to mediate MOMP,[45,46] leading to release of pro-apoptotic proteins including cytochrome *c*.[47,48] The release of cytochrome *c* as a signal will finally activate the executors including Caspase-3 for cell death.[40] Therefore, our findings are consistent with photo-induced lysosomal damage as the basis to induce apoptosis. Nevertheless, based on the observed temperature increases (Figure 6b), photothermal effects could have also contributed to the destruction of cancer cells (Figure 4) and tumors (Figure 6e).

Various light-activated nanoparticle systems are under investigation in relation to cancer imaging and therapy. Based on material type, such systems can generally be classified into semiconductors (e.g., quantum dots (QDs)), metallic (e.g., gold, silver), and organic particles (i.e., carbon nanomaterials such as graphene and fullerene).[49,50] There are certain attractive features with these types of materials such as photostability of QDs, tunable optical properties of QDs and gold nanomaterials, light-induced local surface plasmon resonance effects, and quantum confinement effects due to nanosize (<10nm) of carbon materials that result in their distinct optical properties. Limitations of these materials include cytotoxicity associated with certain constituents of QDs, potential oxidative stress and genotoxicity associated with gold nanoparticles,[51] safety concerns with carbon nanotubes,[52] and short vascular retention time of carbon nanomaterials due to their excretion through the kidneys, which stems from their small size (<10nm).

In comparison to these light-activated nanoparticle systems, the major key advantages of NETs stem from its constituent materials and composition that lead to the distinct properties and capabilities of these particles: (1) As constructs that can be engineered autologously (or from similar blood types), NETs are potentially non-immunogenic, non-toxic, and biocompatible. (2) CD47 is a key membrane glycoprotein expressed in erythrocytes,[53] which impedes phagocytosis. Our previous results[28] indicate that CD47 remains on the surface of NETs, suggesting that NETs may remain shielded from the immune system and have extended retention time within the vasculature; hence, providing their cargo (e.g., ICG) available for delivery to the tumor site over a longer time. Herein, as evidenced by NIR fluorescence imaging and *in vivo* laser irradiation studies, NETs remain available within tumors at 24 hours post intravenous injection. In comparison, the reported half-life of ICG encapsulated in poly(DL-lactic-co-glycolic acid) or liposomal nanoparticles following intravenous injection are, respectively, on the order of approximately five minutes and less than a minute in blood.[19,54] (3) Fabrication of NETs is simple. Particles can be produced within about a day at room temperature and pressure without any complex chemical synthesis procedures, and use of specialized and expensive equipment.

Our results are consistent with the findings by Ren et al in which nanoparticles (≈ 150 nm diameter) comprised of an ICG-bound albumin and perfluorocarbon core encapsulated by an erythrocyte-derived membrane shell were used a photo-therapeutic agent.[55] These investigators also reported that both photothermal and photochemical effects (i.e., production of singlet oxygen) can serve as the basis for destruction of xenograft tumors in mice in response to 808 nm laser irradiation at I_o = 1 W/cm^2 for three minutes.

A synergistic effect of photothermal and photochemical mechanisms indicates that the photophysics of ICG allows for both vibrational relaxations from its excited state electronic states as well as intersystem crossing to a triplet state under the irradiation parameters investigated in this study to ultimately lead to photo-destruction of tumors. The photophysical properties of ICG can be exploited to endow NETs with capabilities for fluorescence imaging and therapeutic effects. In this context, NETs can serve as platforms for light-activated theranostics as applied to a variety of solid tumors. For example, a particularly important clinical application is in relation to ovarian cancer theranostics. Patients with ovarian cancer are most often diagnosed with late stage disease with metastasis to the peritoneum. One of the most important prognostic factors is the degree of cytoreduction at surgery. However, small tumor nodules (< 1 mm) are difficult to detect by current pre-operative imaging methods, or visually during surgery. Furthermore, tumors may reside along critical structures to be removed without inducing significant morbidity. Surgical procedures such as diaphragm stripping, splenectomy, distal pancreatectomy, liver resection, or cholecystectomy may be required to remove such intraperitoneal tumors. NETs can potentially be used as light-activated theranostic nanoprobes during intraoperative procedures to enable visualization of small tumor nodules for surgical removal, or mediate photo-destruction of inoperable tumors.

CONCLUSIONS

We have demonstrated the photo-theranostic capabilities of NETs for fluorescence imaging and photo-destruction of cancer cells, and subcutaneous xenograft tumors in mice. NETs are internalized by cancer cells, and localized to the lysosomes. NETs remain available within tumors at 24 hours post intravenous injection, and mediate the destruction of cancer cells and xenograft tumors through synergistic photochemical and photothermal effects at the irradiation parameters investigated. Our results indicate that NETs are capable of mediating photo-induced tumor destruction initiated by their localization to lysosomes with subsequent activation of Caspase-3, and culminated in tumor apoptosis.

EXPERIMENTAL SECTION

Fabrication of NETs. Erythrocytes were separated from bovine whole blood (Rockland Immunochemicals, Inc., Limerick, PA) by centrifugation (5 minutes, 1,300xg, 4 °C). The supernatant, containing the plasma and buffy coat, was discarded and the resulting packed erythrocytes were washed twice with 1X (310 mOsm, pH ~ 8.0) phosphate buffer saline (PBS). Packed erythrocytes were then subjected to sequential hypotonic treatment with 0.5X PBS (155 mOsm, pH ~ 8.0) and 0.25X PBS (77.5 mOsm, pH ~ 8.0) respectively. The centrifugation process (20,000xg, 15 minutes, 4 °C) was repeated until all the hemoglobin was depleted, resulting in an opaque white pellet containing micron-sized hemoglobin-depleted erythrocyte ghosts (EGs).

To obtain nano-sized EGs, the micron-sized EGs were extruded 10 times through 800 nm polycarbonate porous membranes (Nuclepore Track-Etched Membranes, Whatman, Florham Park, New York), followed by 10 more extrusions through 400 nm polycarbonate membranes, and another 10 times through 200 nm polycarbonate membranes using an extruder (LIPEX Extruder, TRANSFERRA Nanosciences Inc, Burnaby, Canada). To concentrate the nano-sized EGs, 10 ml of nano-sized EGs were centrifuged (99,000xg, 1 hour, 4 °C) and re-suspended in 1 ml of 1X PBS.

To load ICG into nano-sized EGs, 1 ml of nano-sized EGs solution, concentrated by 10 times, was incubated with 3 ml of ICG dissolved in water (at concentration of 2 mg/ml) and 3 ml of hypotonic buffer (Na_2HPO_4/ $Na_2H_2PO_4$, 140 mOsm, pH ~ 5.8), resulting in 6 mg of ICG in 7 ml of the loading buffer. The corresponding concentration of ICG in this loading buffer was ≈ 1.1 mM (considering the molecular weight of ICG as ≈ 775 Da). The suspension was incubated for five minutes at 4 °C in dark, centrifuged at 74,000xg for 30 minutes, and then washed three times using 1X PBS to remove any non-encapsulated ICG. The pellet containing ICG-encapsulated EGs (i.e., NETs) was removed and re-suspended in 1 ml of 1X PBS (4 °C). To avoid saturation in measurements of NIR absorbance values during absorption spectral recordings, this solution of NETs was further diluted by a factor of 80 using 1X PBS. We then acquired the absorption spectrum of the 1:80 diluted solution of NETs.

Next, we proceeded to estimate the free ICG equivalent concentration within the population of NETs [ICG_{NETs}] as follows. We first acquired the absorption spectra of ICG dissolved in water at concentrations in the range of 2-10 μM. We chose water as the solvent since the absorption spectra of NETs resembles that of ICG dissolved in water at concentrations less than ≈ 20 μM. The spectra were then spectrally integrated in the range of 600-900 nm, and the resulting values (A_{int}) were plotted against ICG concentrations to obtain a calibration curve (R^2 = 0.99). We then used the value of A_{int} associated with the 1:80 diluted solution of NETs in conjunction with the calibration curve to estimate [ICG_{NETs}] ≈ 12.25 μM. Finally, we estimated [ICG_{NETs}] for the undiluted NETs to be ≈ 980 μM as the product of 12.25 μM and the dilution factor 80. In a similar fashion, we prepared various dilutions of the NETs solution with values of [ICG_{NETs}] ≈ 2, 10, 18, 36, 72 and 144 μM.

Characterization of NETs. The hydrodynamic diameters of NETs suspended in 1X PBS were measured by dynamic light scattering (DLS) (Zetasizer NanoZS90, Malvern Instruments Ltd, Malvern, United Kingdom). The absorption spectra of NETs ([ICG_{NETs}] ≈ 10 μM) and 13 μM free ICG suspended in 1X PBS were obtained using a UV-visible spectrophotometer (Cary 50 UV-Vis spectrophotometer, Agilent Technologies, Santa Clara, CA) with optical path length of 1 cm. The fluorescence emission spectra of NETs ([ICG_{NETs}] ≈ 2 μM) and 4 μM free ICG were acquired in response to 720 ± 2.5 nm, and recorded using a fluorimeter (Fluorolog-3 spectrofluorometer, Edison, NJ). We normalized the fluorescence emission spectra ($\chi(\lambda)$) as:

$$\chi(\lambda) = \frac{F(\lambda)}{(1\text{-}10^{-A(\lambda_{ex})})} \tag{1}$$

where A and F are the wavelength (λ) dependent absorbance and intensity of the emitted fluorescence light, respectively, and λ_{ex} is the excitation wavelength.

Photostability of NETs. NETs suspended in PBS ([ICG_{NETs}] ≈ 18 μM) and 22 μM of ICG dissolved in PBS were prepared. Samples were then laser-irradiated at 808 nm using intensity (I_o) value of 680 mW/cm^2 (9 mm diameter focal spot) for durations (t_{laser}) ranging between 1-15 minutes. Immediately following each experiment at a given t_{laser}, we acquired the absorption spectra of the samples, and normalized them to the absorbance value at 808 nm ($A(\lambda = 808\text{nm})$) prior to laser irradiation (defined as time t_0).

Detection of singlet oxygen generation. We used 10 µM 1,3-diphenylisobenzofuran (DPBF) as a probe to detect the generation of singlet oxygen ($^1O_2$) in response to 808 nm photo-excitation of 11 µM free ICG or NETs ($[ICG_{NETs}] \approx 18$ µM). DPBF has an absorption peak at 411 nm in DMF.[56] Upon reacting with $^1O_2$, DPBF undergoes 1,4-cycloaddition to form an endoperoxide product, resulting in decreased 411 nm absorption. Samples were irradiated at I_o = 680 mW/cm^2 for 10 seconds. An aliquot of sample was then withdrawn and the absorbance at 411 nm was recorded using a UV-visible spectrophotometer. The absorbance value at 411 nm was normalized to the absorbance value at 411 nm prior to laser irradiation. In the negative control experiment, DPBF solution without NETs or free ICG was irradiated at I_o = 680 mW/cm^2, and the 411 nm absorbance values were determined and normalized as above.

Cell culture. SKBR3 human breast cancer cells (ATCC®, Manassas, VA) were cultured in Rosewell Park Memorial Institute (RPMI) 1640 medium (Mediatech Inc, Manassas, VA) supplemented with 10% fetal bovine serum (FBS) and 1% Penicillin/Streptomycin (Corning Inc., Corning, NY) at 37 °C in 5% humidified CO_2. Cells were used for *in vitro* experiments, and implanted in mice to induce tumors.

Assessment of NETs uptake by SKBR3 cancer cells. We used bright-field and NIR fluorescence imaging, flow cytometry, and laser scanning confocal fluorescence microscopy (LSCFM) to evaluate the uptake of NETs by SKBR3 cancer cells. Cells were cultured in 96-well plates for NIR fluorescence imaging, and 12-well plates for flow cytometry. For LSCFM, cells were grown on poly-l-lysine coated coverslips in 12-well plates. After 24 hours, cells were incubated in RPMI medium containing PBS (negative control), NETs ($[ICG_{NETs}] \approx 36$ µM) or 44 μM free ICG (positive control) for 3 hours. Cells were then washed three times with PBS prior to imaging or flow cytometry.

NIR fluorescence emission (> 770 nm) in response to 740 ± 35 nm excitation by a Nikon Mercury/Xenon arc lamp was captured by an electron multiplier gained charge-coupled device (EM-CCD) camera (Quant EM-CCD, C9100-14 Hamamatsu, Shizuoka-ken, Japan). The camera exposure time was set at 0.7 seconds for NIR fluorescence emission and 0.03 seconds for bright-field images and gain of 1.0. We present falsely colored microscopic images with NIR fluorescent emission due to ICG (red channel) merged with bright-field (gray channel).

For flow cytometry experiments, the RPMI medium was removed, and cells were incubated with trypsin for 5 minutes. After incubation, fresh RPMI was added to halt trypsinization, and cells were subsequently centrifuged at 125xg for 5 minutes. The supernatant was removed, and the pellet was then re-suspended in 1X PBS. A flow cytometer (BD FACSAria cell sorter, San Jose, CA) with photo-excitation at 633 nm and emission collection at > 785 nm was used to measure the NIR signals from cells that had been incubated with PBS, NETs or free ICG. All studies were done using three different samples. During flow cytometry, minimum of ≈10,000 events were counted for each triplicate within the gating region.

For LSCFM experiments, the RPMI medium was removed after incubating the cells with NETs, and cells where then incubated with LysoTracker yellow® HCK-123 (Invitrogen, Carlsbad, CA) for two hours. Immediately after staining with LysoTracker, we fixed and permeated the cells using 4% paraformaldehyde and 2% tween 20, respectively. We then mounted the slide with ProLong™ Gold Antifade containing 4',6-diamidino-2-phenylindole (DAPI) (Invitrogen, Carlsbad, CA) and used a confocal microscope (Leica SP5, Leica Microsystems Inc., Buffalo Grove, IL) with photo-excitation at 405, 488 and 633 nm, corresponding to DAPI, LysoTracker, and ICG absorption respectively. Fluorescence emission were collected at 420-480, 500-610 and > 655 nm, respectively. We present falsely colored microscopic images corresponding to DAPI (blue channel), and LysoTracker yellow emission (green channel), and ICG NIR emission (red channel). For co-localization analysis, we used ImageJ to calculate the pixel intensity correlation using the two methods, Pearson and Costes.[57]

Laser irradiation of SKBR3 cancer cells. To investigate the photo-destructive capability of NETs, SKBR3 cells were cultured in a 96-well. After 24 hours, cells were incubated with RPMI medium containing PBS, free ICG (44, and176 μM)), or NETs (with specific value of $[ICG_{NETs}]$ = 18, 36, 72, or 144 μM) for three hours in dark at 37 °C. After incubation, cells were then washed three times with PBS and fresh medium was added. We subsequently irradiated the cells at 808 nm using I_o values of 680 mW/cm^2 for 15 minutes.

To assess the viability of cells following laser irradiation, cells were incubated in RPMI medium containing 2 μM Calcein-AM and 4 μM Ethidium Homodimer-1 (EthD-1) (ThermoFisher Scientific, Waltham, MA) as the respective live/dead assays for 30 minutes. Cells were then washed with PBS and fluorescently imaged in response to Calcein-AM excitation at 485 ± 35 nm and EthD-1 excitation at 543 ± 22 nm excitation by a Nikon Mercury/Xenon arc lamp. Respective fluorescence emission over the spectral bands of 524 ± 24 nm and 593 ± 40 nm were captured by an EM-CCD camera with exposure time set at 0.03 seconds. We present falsely colored microscopic images with Calcein-AM fluorescent emission (green channel) overlaid with EthD-1 fluorescence emission (red channel). Cell viability in each well was calculated using a fluorescent microplate reader (Molecular Devices FlexStation II 384, Harlow Scientific).

To detect the presence of ROS in response to NIR laser irradiation of SKBR3 cancer cells, we used the molecular probe 2’,7’-dichlorofluorecein diacetate (DCFH-DA) (Sigma-Aldrich, St. Louis, MO). Once the non-fluorescent DCFH-DA is oxidized by ROS, it is converted into a fluorescent molecule 2’,7’-dichlorofluorescein (DCF).[58] In a subset of experiments, cells treated with PBS, 18 μM NETs and 22 μM free ICG for three hours (as described above) were further incubated with 25 μM DCFH-DA in RPMI medium for 30 minutes prior to laser irradiation at the parameters indicated above. Following irradiation, we imaged the cells in bright-field and fluorescence modes. The DCF fluorescence emission (524 ± 24 nm) in response to 485 ± 35 nm excitation by a Nikon Mercury/Xenon arc lamp was captured by an EM-CCD camera. The camera exposure time was set at 0.2 seconds for DCF fluorescence emission and 0.03 seconds for bright-field images and gain of 1.0. We present falsely colored microscopic images with DCF fluorescent emission (green channel) merged with bright-field (gray channel).

To determine if ROS included singlet oxygen ($^1O_2$) as a constituent, we used sodium azide as a $^1O_2$ quencher probe.[38] In a subset of experiments, we pre-treated the SKBR3 cells with DCFH-DA (as described above), washed them after 30 minutes, and then incubated them in RPMI medium containing 50 mM sodium azide for 45 minutes prior to laser irradiation at the indicated parameters above.

Animal study. Female Nu/J mice (20~25 g; 6-8 weeks) were purchased from Jackson Laboratory (Bar Harbor, Maine) and utilized in this study under a protocol approved by the University of California, Riverside Institutional Animal Care and Use Committee (A-20140022). We injected ≈ 1 × 10^7 SKBR3 cancer subcutaneously into the thighs. Mice were monitored until the tumor sizes reached approximately 15 mm^3. The tumor volume was calculated as $D \times d^2/2$, where D and d were the larger and smaller diameter of each tumor.

Tumor-bearing mice were randomly divided into three groups with four animals in each group. Group 1 received PBS injection without laser irradiation. Group 2 received PBS injection and 808 nm laser irradiation using I_o = 680 mW/cm^2 for 10 minutes. Group 3 received NETs [ICG_{NETs} ≈ 980 μM] injection and 808 nm laser irradiation using I_o = 680 mW/cm^2 for 10 minutes. We administered 100 µl of PBS or NETs intravenously via tail-vein injection while the animal was anesthetized. Laser irradiation was performed at 24 hours post injection of PBS or NETs with a beam diameter of 9 mm. We measured the temperature change in response to laser irradiation by inserting a mini-hypodermic thermocouple (0.2 mm thermocouple diameter) (HYP0, OMEGA, Norwalk, CT) connected to a LabQuest® data acquisition system (Vernier, Beaverton, OR) ≈ 1 mm below the skin and about 2 mm outside the laser-irradiated spot. Following the experimental procedures, animals were allowed to recover. We assessed the efficacy of NETs in mediating photo-induced reductions in tumor size by measuring the tumor volumes following each treatment at every two days intervals and for up to 16 days after laser irradiation. We estimated the relative tumor volumes (V/V_o) during this time interval by dividing the volume of each tumor (V) on the measurement day divided by the initial tumor volume (V_o) on the day of laser irradiation. Animals were subsequently euthanized on day 16 following laser irradiation.

In a subset of experiments, an animal from each group was euthanized immediately after laser irradiation. Tumors were removed and frozen at -80 °C for later analysis. Approximately, ≈ 7 days later, tumors were thawed and sectioned in 10 µm thicknesses using a cryostat microtome (CM1950 cryostat, Buffalo Grove, Illinois) and stained with fluorescein isothiocyanate (FITC)-labeled Caspase-3 antibody (BD Biosciences, San Jose, CA) as an established method to assay for cell apoptosis.[59–61] Fluorescent emission (524 ± 24 nm) in response to 485 ± 35 nm excitation by a Nikon Mercury/Xenon arc lamp was captured by an EM-CCD camera with exposure time set at 0.2 seconds. Mean and SDs of the image intensities (n = 5 images) were quantified using ImageJ.

To evaluate the feasibility of NETs in tumor imaging, in a subset of experiments, 100 µl of PBS or NETs [ICG_{NETs} ≈ 980 µM] were administered by tail vein injection. At 24 hours post injection, animals were euthanized, and tumors extracted. Extracted tumors were fluorescently imaged in a dark box. Two light emitting diodes (LEDs) delivering 700 ± 30 nm excitation light were used for illumination. Fluorescence emission was captured using a CCD camera (Pixis 1024B, Roper Scientific, Trenton, NJ) equipped with a long pass filter transmitting wavelengths greater than 810 nm. To prevent pixel saturation, the camera exposure time was set to 90 seconds.

ACKNOWLEDGEMENTS

This study was supported in parts by grants from the National Science Foundation (CBET-1509218), National Cancer Institute at National Institutes of Health (R43-CA210715-A1), University of California Cancer Research Coordinating Committee (5-44189-34912), and University of California, Riverside Office of Research & Economic Development.

REFERENCES

(1) Kim, H.; Chung, K.; Lee, S.; Kim, D. H.; Lee, H. Near-Infrared Light-Responsive Nanomaterials for Cancer Theranostics. *Wiley Interdiscip. Rev.: Nanomed. Nanobiotechnol.* **2016**, *8*, 23-45.

(2) Shan, G.; Weissleder, R.; Hilderbrand, S. A. Upconverting Organic Dye Doped Core-Shell Nano-Composites for Dual-Modality NIR Imaging and Photo-Thermal Therapy. *Theranostics* **2013**, *3*, 267-274.

(3) Lee, M.-Y.; Lee, C.; Jung, H. S.; Jeon, M.; Kim, K. S.; Yun, S. H.; Kim, C.; Hahn, S. K. Biodegradable Photonic Melanoidin for Theranostic Applications. *ACS Nano* **2016**, *10*, 822-831.

(4) Frangioni, J. V. In Vivo Near-Infrared Fluorescence Imaging. *Curr. Opin. Chem. Biol.* **2003**, *7*, 626-634.

(5) Marshall, M. V.; Rasmussen, J. C.; Tan, I.-C.; Aldrich, M. B.; Adams, K. E.; Wang, X.; Fife, C. E.; Maus, E. A.; Smith, L. A.; Sevick-Muraca, E. M. Near-Infrared Fluorescence Imaging in Humans with Indocyanine Green: A Review and Update. *Open Surg. Oncol. J.* **2010**, *2*, 12-25.

(6) Roessler, K.; Krawagna, M.; Dorfler, A.; Buchfelder, M.; Ganslandt, O. Essentials in Intraoperative Indocyanine Green Videoangiography Assessment for Intracranial Aneurysm Surgery: Conclusions from 295 Consecutively Clipped Aneurysms and Review of the Literature. *Neurosurg. Focus* **2014**, *36*, E7 (pp 7).

(7) Crane, L. M. A.; Themelis, G.; Arts, H. J. G.; Buddingh, K. T.; Brouwers, A. H.; Ntziachristos, V.; van Dam, G. M.; van der Zee, A. G. J. Intraoperative Near-Infrared Fluorescence Imaging for Sentinel Lymph Node Detection in Vulvar Cancer: First Clinical Results. *Gynecol. Oncol*. **2011**, *120*, 291-295.

(8) Hirche, C.; Murawa, D.; Mohr, Z.; Kneif, S.; Hunerbein, M. ICG Fluorescence-Guided Sentinel Node Biopsy for Axillary Nodal Staging in Breast Cancer. *Breast Cancer Res. Treat*. **2010**, *121*, 373-378.

(9) Sevick-Muraca, E. M.; Sharma, R.; Rasmussen, J. C.; Marshall, M. V.; Wendt, J. A.; Pham, H. Q.; Bonefas, E.; Houston, J. P.; Sampath, L.; Adams, K. E.; Blanchard, D. K; Fisher, R. E.; Chiang, S. B.; Elledge, R.; Mawad, M. E. Imaging of Lymph Flow in Breast Cancer Patients after Microdose Administration of a Near-Infrared Fluorophore: Feasibility Study. *Radiology* **2008**, *246*, 734-741.

(10) Verbeek, F. P. R.; Troyan, S. L.; Mieog, J. S. D.; Liefers, G.-J.; Moffitt, L. A.; Rosenberg, M.; Hirshfield-Bartek, J.; Gioux, S.; van de Velde, C. J. H.; Vahrmeijer, A. L.;

Frangioni, J. V. Near-Infrared Fluorescence Sentinel Lymph Node Mapping in Breast Cancer: A Multicenter Experience. *Breast Cancer Res. Treat.* **2014**, *143*, 333-342.

(11) Zaidi, H. A.; Abla, A. A.; Nakaji, P.; Chowdhry, S. A.; Albuquerque, F. C.; Spetzler, R. F. Indocyanine Green Angiography in the Surgical Management of Cerebral Arteriovenous Malformations: Lessons Learned in 130 Consecutive Cases. *Neurosurgery* **2014**, *10 Suppl 2*, 246-251.

(12) Liggett, P. E.; Lavaque, A. J.; Chaudhry, N. A.; Jablon, E. P.; Quiroz-Mercado, H. Preliminary Results of Combined Simultaneous Transpupillary Thermotherapy and ICG-Based Photodynamic Therapy for Choroidal Melanoma. *Ophthal. Surg. Las. Im.* **2005**, *36*, 463-470.

(13) Montazerabadi, A. R.; Sazgarnia, A.; Bahreyni-Toosi, M. H.; Ahmadi, A.; Aledavood, A. The Effects of Combined Treatment with Ionizing Radiation and Indocyanine Green-Mediated Photodynamic Therapy on Breast Cancer Cells. *J. Photochem. Photobiol., B.* **2012**, *109*, 42-49.

(14) Klein, A.; Baumler, H.; Buschmann, M.; Landthaler, M.; Babilas, P. A Randomized Controlled Trial to Optimize Indocyanine Green-Augmented Diode Laser Therapy of Capillary Malformations. *Lasers Surg. Med.* **2013**, *45*, 216-224.

(15) Kirchherr, A. K.; Briel, A.; Mäder, K. Stabilization of Indocyanine Green by Encapsulation within Micellar Systems. *Mol. Pharmaceutics* **2009**, *6*, 480-491.

(16) Wu, L.; Fang, S.; Shi, S.; Deng, J.; Liu, B.; Cai, L. Hybrid Polypeptide Micelles Loading Indocyanine Green for Tumor Imaging and Photothermal Effect Study. *Biomacromolecules* **2013**, *14*, 3027-3033.

(17) Kraft, J. C.; Ho, R. J. Interactions of Indocyanine Green and Lipid in Enhancing Near-Infrared Fluorescence Properties: The Basis for Near-Infrared Imaging in Vivo. *Biochemistry* **2014**, *53*, 1275-1283.

(18) Bahmani, B.; Gupta, S.; Upadhyayula, S.; Vullev, V. I.; Anvari, B. Effect of Polyethylene Glycol Coatings on Uptake of Indocyanine Green Loaded Nanocapsules by Human Spleen Macrophages in Vitro. *J. Biomed. Opt.* **2011**, *16*, 51303 (pp 10).

(19) Saxena, V.; Sadoqi, M.; Shao, J. Polymeric Nanoparticulate Delivery System for Indocyanine Green: Biodistribution in Healthy Mice. *Int. J. Pharm. (Amsterdam, Neth.)* **2006**, *308*, 200-204.

(20) Sharma, P.; Bengtsson, N. E.; Walter, G. A.; Sohn, H.-B.; Zhou, G.; Iwakuma, N.; Zeng, H.; Grobmyer, S. R.; Scott, E. W.; Moudgil, B. M. Gadolinium-Doped Silica Nanoparticles Encapsulating Indocyanine Green for Near Infrared and Magnetic Resonance Imaging. *Small* **2012**, *8*, 2856-2868.

(21) Yoo, J.-W.; Irvine, D. J.; Discher, D. E.; Mitragotri, S. Bio-Inspired, Bioengineered and Biomimetic Drug Delivery Carriers. *Nat. Rev. Drug Discov.* **2011**, *10*, 521-535.

(22) Muzykantov, V. R. Drug Delivery by Red Blood Cells: Vascular Carriers Designed by Mother Nature. *Expert Opin. Drug Delivery* **2010**, *7*, 403-427.

(23) Rao, L.; Meng, Q.-F.; Bu, L.-L.; Cai, B.; Huang, Q.; Sun, Z. J.; Zhang, W. F.; Li, A.; Guo, S.-S.; Liu, W.; Wang, T.-H.; Zhao, X.-Z., Erythrocyte Membrane-Coated Upconversion Nanoparticles with Minimal Protein Adsorption for Enhanced Tumor Imaging. *ACS Appl. Mater. Interfaces* **2017**, *9*, 2159-2168.

(24) Piao, J. G.; Wang, L.; Gao, F.; You, Y. Z.; Xiong, Y.; Yang, L., Erythrocyte Membrane Is an Alternative Coating to Polyethylene Glycol for Prolonging the Circulation Lifetime of Gold Nanocages for Photothermal Therapy. *ACS Nano* **2014**, *8*, 10414-10425.

(25) Peng, J.; Yang, Q.; Li, W. T.; Tan, L. W.; Xiao, Y.; Chen, L.; Hao, Y.; Qian, Z. Erythrocyte-Membrane-Coated Prussian Blue/Manganese Dioxide Nanoparticles as H2O2-

Responsive Oxygen Generators to Enhance Cancer Chemotherapy/Photothermal Therapy. *ACS Appl. Mater. Interfaces* **2017**, *9*, 44410-44422.

(26) Hu, C.-M. J.; Zhang, L.; Aryal, S.; Cheung, C.; Fang, R. H.; Zhang, L. Erythrocyte Membrane-Camouflaged Polymeric Nanoparticles as a Biomimetic Delivery Platform. *Proc. Natl. Acad. Sci. U.S.A.* **2011**, *108*, 10980-10985.

(27) , B.; Bacon, D.; Anvari, B. Erythrocyte-Derived Photo-Theranostic Agents: Hybrid Nano-Vesicles Containing Indocyanine Green for Near Infrared Imaging and Therapeutic Applications. *Sci. Rep.* **2013**, *3*, 2180 (pp 7).

(28) Mac, J. T.; Nuñez, V.; Burns, J. M.; Guerrero, Y. A.; Vullev, V. I.; Anvari, B. Erythrocyte-Derived Nano-Probes Functionalized with Antibodies for Targeted Near Infrared Fluorescence Imaging of Cancer Cells. *Biomed. Opt. Express* **2016**, *7*, 1311-1322.

(29) Nobbmann, U.; Morfesis, A. Light Scattering and Nanoparticles. *Mater. Today* **2009**, *12*, 52-54.

(30) Nakamura, H.; Jun, F.; Maeda, H. Development of Next-Generation Macromolecular Drugs Based on the EPR Effect: Challenges and Pitfalls. *Expert Opin. Drug Delivery* **2015**, *12*, 53-64.

(31) Torchilin, V. Tumor Delivery of Macromolecular Drugs Based on the EPR Effect. *Adv. Drug Delivery Rev.* **2011**, *63*, 131-135.

(32) Jung, B.; Vullev, V. I.; Anvari, B. Revisiting Indocyanine Green: Effects of Serum and Physiological Temperature on Absorption and Fluorescence Characteristics. *IEEE J. Sel. Top. Quantum Electron.* **2014**, *20*, 149-157.

(33) Burns, J. M.; Saager, R.; Majaron, B.; Jia, W.; Anvari, B. Optical Properties of Biomimetic Probes Engineered from Erythrocytes. *Nanotechnology* **2017**, *28*, 35101 (pp 12).

(34) Sibrian-Vazquez, M.; Escobedo, J. O.; Lowry, M.; Fronczek, F. R.; Strongin, R. M. Field Effects Induce Bathochromic Shifts in Xanthene Dyes. *J. Am. Chem. Soc.* **2012**, *134*, 10502-10508.

(35) Philip, R.; Penzkofer, A.; Baumler, W.; Szeimies, R. M.; Abels, C. Absorption and Fluorescence Spectroscopic Investigation of Indocyanine Green. *J. Photochem. Photobiol., A* **1996**, *96*, 137-148.

(36) Tan, X.; Luo, S.; Long, L.; Wang, Y.; Wang, D.; Fang, S.; Ouyang, Q.; Su, Y.; Cheng, T.; Shi, C. Structure-Guided Design and Synthesis of a Mitochondria-Targeting Near-Infrared Fluorophore with Multimodal Therapeutic Activities. *Adv. Mater.* **2017**, *29*, 1704196 (pp 9).

(37) Ranran, G.; Peng, H.; Tian, Y.; Shen, S.; Yang, W. Mitochondria-Targeting Magnetic Composite Nanoparticles for Enhanced Phototherapy of Cancer. *Small* **2016**, *12*, 4541-4552.

(38) Li, M. Y.; Cline, C. S.; Koker, E. B.; Carmichael, H. H.; Chingnell, C. F.; Bilski, P. Quenching of Singlet Molecular Oxygen (1O2) by Azide Anion in Solvent Mixtures. *Photochem. Photobiol.* **2001**, *74*, 760-764.

(39) Kessel, D.; Luo, Y. Intracellular Sites of Photodamage as a Factor in Apoptotic Cell Death. *J. Porphyrins Phthalocyanines* **2001**, *5*, 181-184.

(40) Reiners Jr, J. J.; Caruso, J. A.; Mathieu, P.; Chelladurai, B.; Yin, X.-M.; Kessel, D. Release of Cytochrome C and Activation of Pro-Caspase-9 Following Lysosomal Photodamage Involves Bid Cleavage. *Cell Death Differ.* **2002**, *9*, 934-944.

(41) Wang, X. The Expanding Role of Mitochondria in Apoptosis. *Genes Dev* **2001**, *15*, 2922-2933.

(42) Wang, Y.; Tjandra, N. Structural Insights of tBid, the Caspase-8-Activated Bid, and its BH3 Domain. *J. Biol. Chem*. **2013**, *288*, 35840-35851.

(43) Epand, R. F.; Martinou, J.-C.; Fornallaz-Mulhauser, M.; Hughes, D. W.; Epand, R. M. The Apoptotic Protein tBid Promotes Leakage by Altering Membrane Curvature. *J. Biol. Chem*. **2002**, *277*, 32632-32639.

(44) Grinberg, M.; Sarig, R.; Zaltsman, Y.; Frumkin, D.; Grammatikakis, N.; Reuveny, E.; Gross, A. tBID Homooligomerizes in the Mitochondrial Membrane to Induce Apoptosis. *J. Biol. Chem.* **2002**, *277*, 12237-12245.

(45) Lovell, J. F.; Billen, L. P.; Bindner, S.; Shamas-Din, A.; Fradin, C.; Leber, B.; Andrews, D. W. Membrane Binding by tBid Initiates an Ordered Series of Events Culminating in Membrane Permeabilization by Bax. *Cell* **2008**, *135*, 1074-1084.

(46) Ott, M.; Norberg, E.; Zhivotovsky, B.; Orrenius, S. Mitochondrial Targeting of tBid/Bax: A Role for the TOM Complex? *Cell Death Differ.* **2009**, *16*, 1075-1082.

(47) Bogner, C.; Leber, B.; Andrews, D. W. Apoptosis: Embedded in Membranes. *Curr. Opin. Cell Biol.* **2010**, *22*, 845-851.

(48) Kim, H.; Tu, H.-C.; Ren, D.; Takeuchi, O.; Jeffers, J. R.; Zambetti, G. P.; Hsieh, J. J.-D.; Cheng, E. H.-Y. Stepwise Activation of BAX and BAK by tBID, BIM, and PUMA Initiates Mitochondrial Apoptosis. *Mol. Cell* **2009**, *36*, 487-499.

(49) Ai, X.; Mu, J.; Xing, B. Recent Advances of Light-Mediated Theranostics. *Theranostics.* **2016**, *6*, 2439-2457.

(50) Hyemin, K.; Beack, S.; Han, S.; Myeonghwan, S.; Lee, T.; Park, Y.; Kim, K. S.; Yetisen, A. K.; Yun, S. H.; Kwon, W.; Hahn S. K.; Multifunctional Photonic Nanomaterials for Diagnostic, Therapeutic, and Theranostic Applications. *Adv Mater.* **2018**, *30*, 1701460 (pp 30).

(51) Jiang, X.-M.; Wang, L.-M.; Wang, J.; Chen, C.-Y. Gold Nanomaterials: Preparation, Chemical Modification, Biomedical Applications and Potential Risk Assessment. *Appl Biochem Biotechnol.* **2012**, *166*, 1533-1551.

(52) Liu, Y.; Zhao, Y.; Sun, B.; Chen, C. Understanding the Toxicity of Carbon Nanotubes. *Acc. Chem. Res.* **2013**, *46*, 702-713.

(53) Oldenborg, P.-A.; Zheleznyak, A.; Fang, Y.-F.; Lagenaur, C. F.; Gresham, H. D.; Lindberg, F. P. Role of CD47 as a Marker of Self on Red Blood Cells. *Science* **2000**, *288*, 2051-2054.

(54) Hwang, Y.; Yoon, H.; Choe, K.; Ahn, J.; Jung, J. H.; Park, J.-H.; Kim, P. In Vivo Cellular-Level Real-Time Pharmacokinetic Imaging of Free-Form and Liposomal Indocyanine Green in Liver. *Biomed. Opt. Express.* **2017**, *8*, 4706-4716.

(55) Ren, H.; Liu, J.; Li, Y.; Wang, H.; Ge, S.; Yuan, A.; Hu, Y.; Wu, J. Oxygen Self-Enriched Nanoparticles Functionalized with Erythrocyte Membranes for Long Circulation and Enhanced Phototherapy. *Acta Biomater.* **2017**, *59*, 269-282.

(56) Spiller, W.; Kliesch, H.; Wöhrle, D.; Hackbarth, S.; Röder, B.; Schnurpfeil, G. Singlet Oxygen Quantum Yields of Different Photosensitizers in Polar Solvents and Micellar Solutions. *J. Porphyrins Phthalocyanines* **1998**, *2*, 145-158.

(57) Costes, S. V.; Daelemans, D.; Cho, E. H.; Dobbin, Z.; Pavlakis, G.; Lockett, S. Automatic and Quantitative Measurement of Protein-Protein Colocalization in Live Cells. *Biophys. J.* **2004**, *86*, 3993-4003.

(58) Kalyanaraman, B.; Darley-Usmar, V.; Davies, K.; Dennery, P.; Forman, H.; Grisham, M.; Mann, G.; Moore, K.; Roberts II, L.; Ischiropoulos, H. Measuring Reactive Oxygen and Nitrogen Species with Fluorescent Probes: Challenges and Limitations. *Free Radical Biol. Med.* **2012**, *52*, 1-6.

(59) Yu, Z.; Sun, Q.; Pan, W.; Li, N.; Tang, B. A Near-Infrared Triggered Nanophotosensitizer Inducing Domino Effect on Mitochondrial Reactive Oxygen Species Burst for Cancer Therapy. *ACS Nano* **2015**, *9*, 11064-11074.

(60) Nam, G.; Rangasamy, S.; Ju, H.; Samson, A. A. S.; Song, J. M. Cell Death Mechanistic Study of Photodynamic Therapy Against Breast Cancer Cells Utilizing Liposomal Delivery of 5,10,15,20-tetrakis(benzo[b]thiophene) Porphyrin. *J. Photochem. Photobiol., B* **2017**, *166*, 116-125.

(61) Rizvi, I.; Anbil, S.; Alagic, N.; Celli, J. P.; Zheng, L. Z.; Palanisami, A.; Glidden, M. D.; Pogue, B. W.; Hasan, T. PDT Dose Parameters Impact Tumoricidal Durability and Cell Death Pathways in a 3D Ovarian Cancer Model. *Photochem. Photobiol.* **2013**, *89*, 942-952.